PHYSICAL REVIEW B **97**, 155120 (2018)

Probing the Fermi surface and magnetotransport properties of $MoAs_2$

Ratnadwip Singha,[1] Arnab Pariari,[1] Gaurav Kumar Gupta,[2] Tanmoy Das,[2] and Prabhat Mandal[1]
[1]*Saha Institute of Nuclear Physics, HBNI, 1/AF Bidhannagar, Calcutta 700 064, India*
[2]*Department of Physics, Indian Institute of Science, Bangalore 560 012, India*

(Received 23 August 2017; published 9 April 2018)

Transition-metal dipnictides (TMDs) have recently been identified as possible candidates to host a topology-protected electronic band structure. These materials belong to an isostructural family and show several exotic transport properties. Especially, the large values of magnetoresistance (MR) and carrier mobility have drawn significant attention from the perspective of technological applications. In this paper, we investigate the magnetotransport and Fermi surface properties of single-crystalline $MoAs_2$, another member of this group of compounds. A field-induced resistivity plateau and a large MR have been observed, which are comparable to those in several topological systems. Interestingly, in contrast to other isostructural materials, the carrier density in $MoAs_2$ is quite high and shows single-band-dominated transport. The Fermi pockets, which have been identified from the quantum oscillation, are the largest among the members of this group and have significant anisotropy with crystallographic direction. Our first-principles calculations reveal a substantial difference between the band structures of $MoAs_2$ and that of other TMDs. The calculated Fermi surface consists of one electron pocket and another "open-orbit" hole pocket, which has not been observed in TMDs so far.

DOI: 10.1103/PhysRevB.97.155120

I. INTRODUCTION

The emergence of topological materials in condensed-matter physics has introduced a completely new perspective in which the materials are characterized in terms of the topology of their electronic band structure and the physics is dictated by the inherent symmetries of the system. These materials are the subject of extensive theoretical and experimental studies and continue to reveal new exotic topological phases of matter. While the discovery of topological insulators (TIs) marks the beginning of this field [1–3], subsequent realizations of Dirac, Weyl, and nodal line semimetals [4–9] have further enriched this field of research. Conducting surface and insulating bulk states are the distinctive features of TIs, whereas the bulk conduction band and valence band cross at either fourfold-/twofold-degenerate discrete points (Dirac/Weyl points) or along a one-dimensional line (the nodal line) in topological semimetals (TSMs). In the vicinity of these band crossings, the dynamics of the quasiparticle excitations is described by relativistic equations of motion. Apart from the opportunity to explore the novel physics of relativistic particles, topological systems have also caught researchers' attention due to their unique transport properties [10–12], which can have a huge impact on technological applications [13,14]. However, the real challenge lies in finding new materials which are suitable for both basic research and technological use.

The family of transition-metal dipnictides (XPn_2; $X =$ Ta, Nb, $Pn =$ P, As, Sb) has recently been proposed as ideal candidates for investigating topology-protected electronic systems [15]. These materials possess identical electronic band structure and host multiple band anticrossings near the Fermi level. In the absence of spin-orbit coupling (SOC), these anticrossings form a nodal line in **k** space. However, with the inclusion of SOC, the nodal line is gapped out, leading to only isolated electron and hole pockets. Several magnetotransport studies have been reported for different members of this family [16–20]. Although the results have been seen to vary slightly for different systems, they all show low-temperature resistivity saturation, large magnetoresistance (MR), and high carrier mobility, which are some of the characteristics of TSMs. On the other hand, in these reports [16–20], the magnetotransport properties are often attributed to the compensated electron-hole density rather than any nontrivial band topology.

Here, we investigate the transport properties of single-crystalline $MoAs_2$, a member of the XPn_2 family. We have obtained large and anisotropic MR and a robust low-temperature resistivity plateau in spite of quite high carrier density and single-band-dominated transport. The Fermi surface of the material is analyzed with de Haas–van Alphen (dHvA) oscillation. The band structure calculation reveals a large electron-type Fermi pocket along with another "open-orbit," hole-type Fermi surface.

II. SINGLE-CRYSTAL GROWTH AND EXPERIMENTAL DETAILS

The single crystals of $MoAs_2$ were grown using the iodine vapor transport method [21]. First, the polycrystalline powder was synthesized from elemental Mo (Alfa Aesar 99.95%) and As (Alfa Aesar 99.9999%) in an evacuated quartz tube at 950 °C for 5 days. The powder and iodine (5 mg/cm^3) were sealed in another quartz tube under vacuum and put in a gradient furnace for 7 days. The hotter end of the tube, containing the polycrystalline powder, was kept at 950 °C, whereas the other end was maintained at 900 °C. Needlelike single crystals with typical dimensions of $1 \times 0.8 \times 0.4$ mm^3 were obtained at the cold end. The crystals were characterized using the powder x-ray diffraction technique in a Rigaku x-ray diffractometer (TTRAX III). The transport measurements were

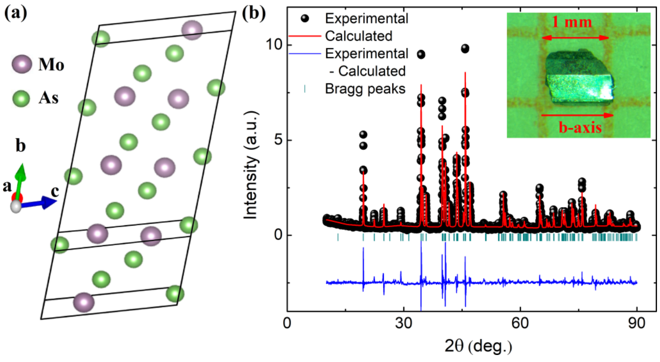

FIG. 1. (a) Crystal structure of $MoAs_2$. (b) X-ray diffraction spectra of the powdered $MoAs_2$ single crystals. The inset shows a typical crystal grown along the crystallographic *b* axis.

performed in a 9-T physical property measurement system (Quantum Design) by using the ac-transport option and rotating the sample holder. The electrical contacts were made using gold wires and conducting silver paint (Leitsilber 200N) in a four-probe configuration. Magnetization measurements were done in a 7-T superconducting quantum interference device–vibrating-sample magnetometer MPMS3 (Quantum Design).

III. COMPUTATIONAL DETAILS

Band structure calculations are performed using density functional theory within the local-density approximation (LDA) exchange correlation as implemented in the Vienna Ab initio Simulation Package (VASP) [22]. Projector augmented-wave (PAW) pseudopotentials are used to describe the core electron in the calculation [23]. The LDA+U method is used to deal with the strong correlation in this material, with the standard value of $U = 2.4$ eV for the correlated Mo 4d orbitals. The electronic wave function is expanded using a plane wave up to a cutoff energy of 224.584 eV. Brillouin zone sampling is done by using an $(8 \times 8 \times 8)$ Monkhorst-Pack **k** grid. Both the atomic position and cell parameters are allowed to relax until the forces on each atom are less than 0.01 eV/Å.

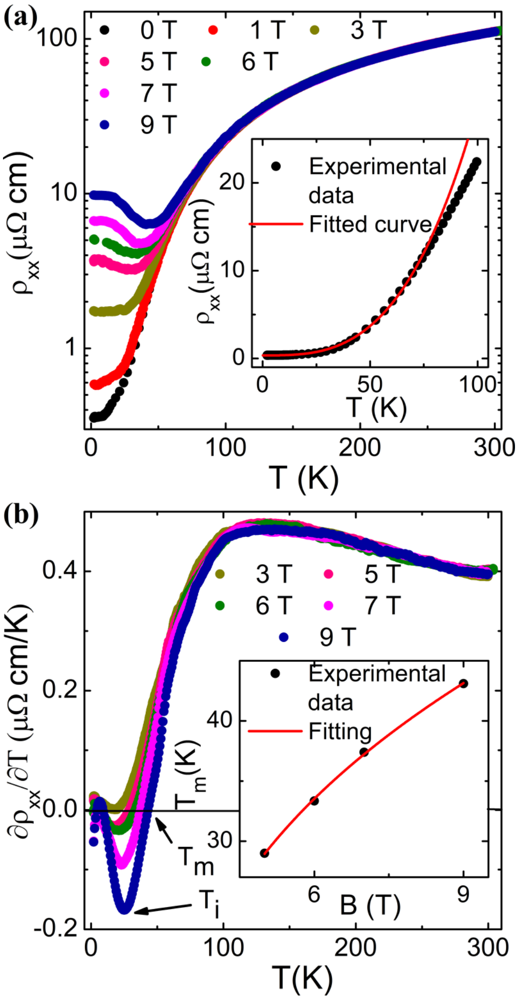

FIG. 2. (a) Temperature dependence of resistivity at different magnetic field strengths, applied along the *c* axis. The inset shows the low-temperature region of the zero-field resistivity, fitted using a $\rho_{xx}(T) = a + bT^n$ type relation. (b) $\partial\rho_{xx}/\partial T$ vs temperature curves at different magnetic fields, which reveal two characteristic temperatures, T_m (zero-crossing point) and T_i (point of minima). The field dependence of the metal-to-semiconductorlike crossover temperature T_m is shown in the inset.

IV. RESULTS AND DISCUSSION

$MoAs_2$ crystallizes in the $OsGe_2$-type structure with monoclinic space group $C12/m1$ [24]. The primitive unit cell contains two inequivalent Mo atoms. The crystal structure is shown in Fig. 1(a). Each molybdenum atom is surrounded by six arsenic atoms, which form a trigonal prism. A typical single crystal of $MoAs_2$ is shown in the inset of Fig. 1(b) with appropriate length scale. The needlelike crystals of the XPn_2 family preferably grow along the *b* axis [17]. Here, the top facet of the crystal corresponds to the (001) plane, whereas the inclined side facet is the (201) plane. The long edge, shared between these two crystal planes, indicates the direction of the crystallographic *b* axis [17]. For simplicity, we discuss the results along three mutually perpendicular crystallographic directions, the *b* and *c* [perpendicular to the (001) plane] and $b \times c$ axes, throughout this report. The x-ray diffraction (XRD) spectrum of powdered crystals is shown in Fig. 1(b). The obtained spectrum confirms the phase purity of the grown crystals and the absence of any impurity. The XRD pattern was analyzed with Rietveld structural refinement using the FULLPROF software package. The refined parameters, $a = 9.062(5)$ Å, $b = 3.296(2)$ Å, $c = 7.715(4)$ Å, and $\beta = 119.3(2)^\circ$, are in agreement with an earlier report [24].

The resistivity measurements on as-grown crystals were done with the current along the *b* axis. As illustrated in Fig. 2(a), the temperature dependence of the resistivity $\rho_{xx}(T)$ shows metallic character throughout the measured temperature range. ρ_{xx} becomes as small as $\sim$0.35 $\mu\Omega$ cm at 2 K and yields a residual resistivity ratio [RRR = $\rho_{xx}(300\,\mathrm{K})/\rho_{xx}(2\,\mathrm{K})$] of $\sim$312. Very low residual resistivity and high RRR are the clear signatures of the high quality of the single crystals. While the resistivity decreases linearly with temperature from 300 K, the experimental data can be fitted well with a $\rho_{xx}(T) = a + bT^n$ ($n \sim 3$) type relation below 75 K

[Fig. 2(a), inset]. A deviation from the value $n = 2$ typically indicates a drift from the pure-electron-correlation-dominated scattering mechanism, whereas $n = 5$ reveals conventional electron-phonon scattering [25]. A similar deviation from the T^2 dependence at low temperature has also been observed in the topological semimetals LaBi ($n = 3$), LaSb ($n = 4$), and ZrSiS ($n = 3$) and in elemental yttrium and transition-metal carbide [12,26–29]. Although the origin of such behavior is not yet settled unambiguously, it is often attributed to the interband electron-phonon scattering [27,29]. When the magnetic field is applied, the low-temperature resistivity shows an enhancement followed by a saturation behavior. The field-induced metal-to-semiconductorlike crossover and resistivity plateau have been seen to be generic features of TSMs [10–12]. Although two different mechanisms based on the field-induced gap-opening model [30] and Kohler scaling analysis [31,32] have been proposed, the actual origin of such behavior has yet to be established unambiguously. Nevertheless, two characteristic temperatures (T_m and T_i) can be identified from the $\partial\rho_{xx}/\partial T$ curves in Fig. 2(b). T_m is the crossover temperature and is indicated by the zero-crossing point of the $\partial\rho_{xx}/\partial T$ curve, whereas T_i is the point of minima in the $\partial\rho_{xx}/\partial T$ vs T plot. T_i corresponds to the inflection point in $\rho_{xx}(T)$, below which resistivity saturation starts to occur. As shown in the inset of Fig. 2(b), T_m increases monotonically with applied field strength and follows a $(B - B_0)^{1/3}$ type relation. On the other hand, T_i shows a weak field dependence.

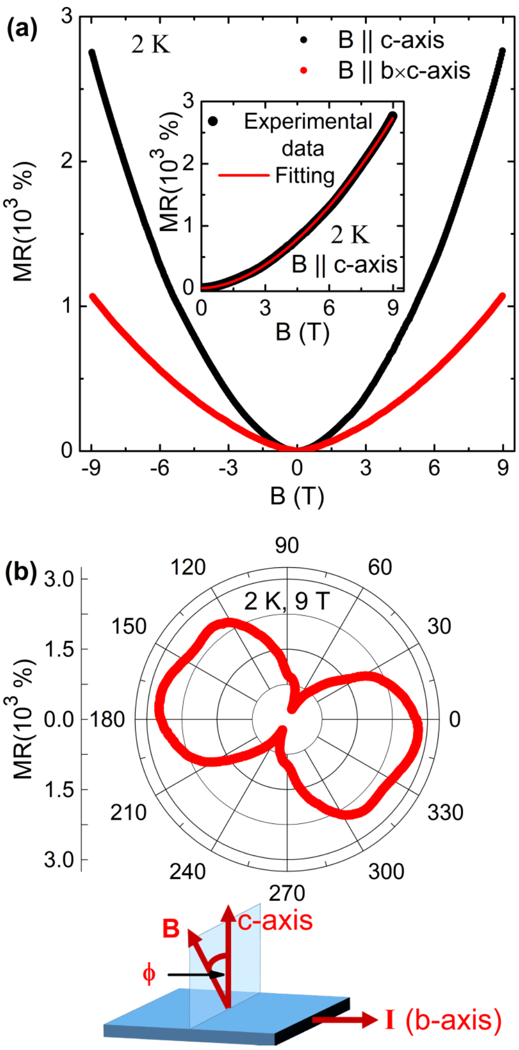

FIG. 3. (a) Transverse magnetoresistance (MR) of MoAs$_2$ at 2 K when current is along the *b* axis and magnetic field is applied along two mutually perpendicular crystallographic directions, the *b* axis and the $b \times c$ axis. The fitting in the inset illustrates nearly the parabolic field dependence of MR. (b) Polar plot of MR when the magnetic field is rotated in the plane perpendicular to the *b* axis. The experimental setup is shown schematically in the inset.

Next, we measured the transverse MR of the sample with the current along the *b* axis and magnetic field along the *c* axis in the temperature range from 300 down to 2 K. At 9 T and 2 K, a very large and nonsaturation MR of approximately $2.75 \times 10^3\%$ was obtained [Fig. 3(a)]. The observed value is smaller than that of other members of the XPn_2 family [16,17,19,20] but is comparable to several other TSMs [33–36]. With increasing temperature, MR decreases drastically and becomes less than 1% at 300 K. As shown in the inset for a representative temperature, the MR curve obeys almost quadratic magnetic field dependence (MR $\propto B^{1.8}$). Keeping the current direction unaltered, when the field is applied along the $b \times c$ axis, the MR changes significantly and becomes approximately $1.1 \times 10^3\%$ at 2 K and 9 T. To map the complete directional dependence of the magnetotransport properties, we have rotated the magnetic field in the plane perpendicular to the current while keeping the current always along the *b* axis. The calculated MR is shown as a polar plot in Fig. 3(b). The MR shows a twofold rotational symmetry with butterflylike strong anisotropy. At 2 K and 9-T magnetic field, the maximum value is about $2.8 \times 10^3\%$ at $\sim170^\circ$ (and $\sim350^\circ$), whereas the MR becomes as small as 250% at around 65° (and $\sim245^\circ$). The large anisotropic ratio (~11.2) indicates the highly anisotropic Fermi surface in MoAs$_2$. In addition to this twofold symmetry pattern, dips and kinks in the MR value have been observed at $\sim145^\circ$ (and $\sim325^\circ$) and $\sim90^\circ$ (and $\sim270^\circ$), respectively. They may be due to some higher-order texturing, which vanishes quickly with increasing temperature. Butterflylike anisotropic patterns in MR have been previously observed in underdoped cuprate superconductors and a manganite system as well as in the recently discovered TSM ZrSiS [37–39]. However, in these systems, higher-order textures are seen to be more robust than in MoAs$_2$. The experimental data can be fitted to a great extent (see Fig. 8 in the Appendix) assuming contributions from both twofold and fourfold symmetries [37], $\mathrm{MR}(\phi) = C + A_2 \sin[2(\phi - \phi_2)] + A_4 \sin[4(\phi - \phi_4)]$, where A_2 (A_4) and ϕ_2 (ϕ_4) are the amplitude and phase of the twofold (fourfold) symmetry, respectively. C is an arbitrary constant. The overall pattern in Fig. 3(b) appears to be tilted with respect to the crystallographic directions. This may be the consequence of the complex Fermi surface and the relative contributions of different Fermi pockets in the transport properties [40].

We also measured the MR by changing the angle between the current and magnetic field, i.e., by rotating the field along the *bc* plane. Although the MR reaches its minimum with parallel electric and magnetic field (longitudinal configuration) as expected, it still remains positive. In an earlier study [41], negative longitudinal magnetoresistance (LMR) was reported for MoAs$_2$ below 40 K. Negative LMR is often considered a signature of the Adler-Bell-Jackiw chiral anomaly [42,43],

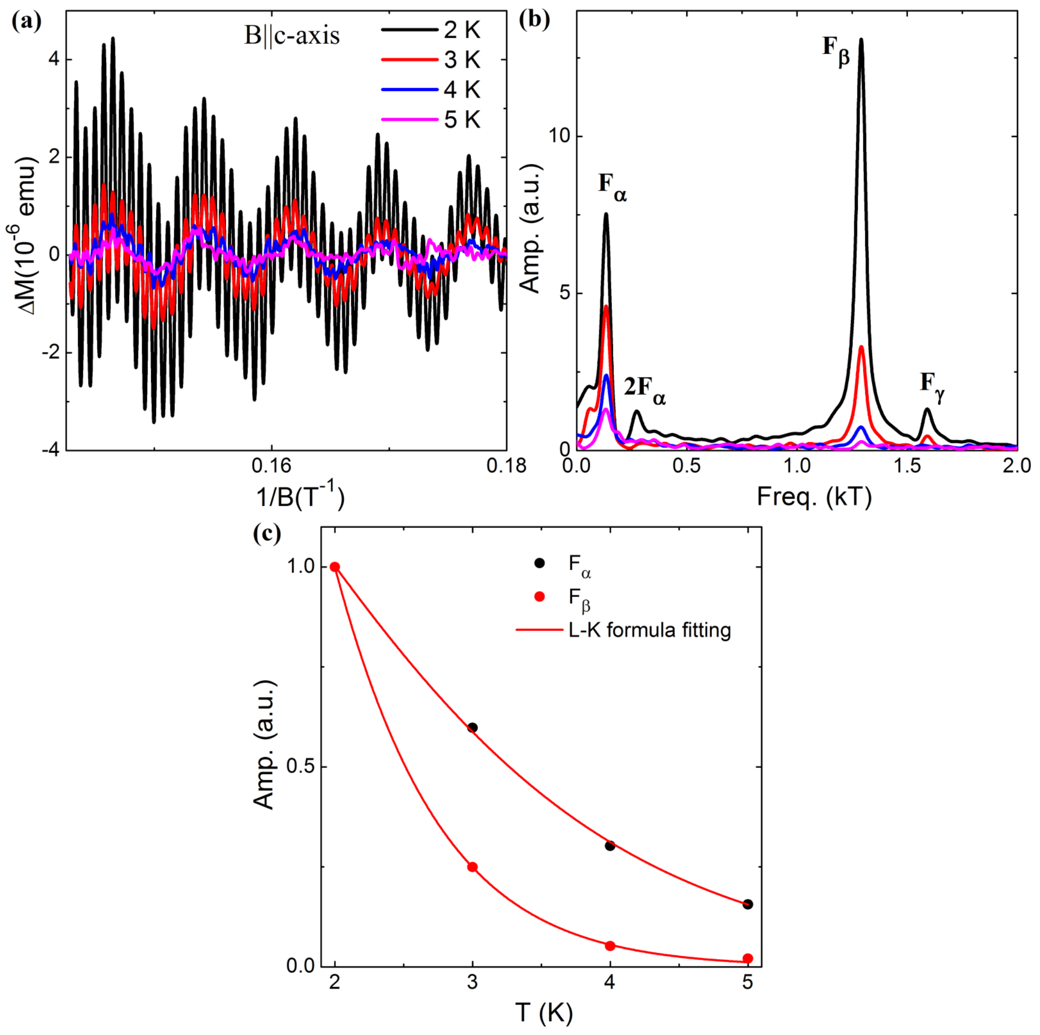

FIG. 4. (a) The de Haas–van Alphen (dHvA) oscillation in the magnetization measurement of $MoAs_2$ for magnetic field along the c axis at different representative temperatures. (b) The fast Fourier transform spectra of the dHvA oscillation. (c) Temperature dependence of the oscillation amplitude for two Fermi pockets, F_α and F_β.

which originates from the charge pumping between two Weyl nodes of opposite chirality. However, negative LMR can also appear because of the current jetting effect, i.e., due to an inhomogeneous current distribution inside the sample [44]. In fact, it has been shown for $TaAs_2$ that this effect can easily be suppressed by changing the current and voltage lead positions [18]. Nevertheless, chiral-anomaly-induced negative LMR has a specific temperature and magnetic field dependence [42], which is distinct from the current jetting effect. For $MoAs_2$, we did not find any negative MR, even when we changed the angle between the current and magnetic field by a few degrees to compensate for any possible misalignment.

TABLE I. Fermi surface parameters extracted from dHvA oscillations. A'_F represents the theoretically calculated Fermi surface cross sections.

Configuration	F (T)	A_F (10^{-3} Å^{-2})	k_F (10^{-3} Å^{-1})	m^* (units of m_0)	v_F (10^5 m/s)	A'_F (10^{-3} Å^{-2})
$B \parallel c$ axis	134(3)	12.8(3)	63.8(8)	0.37(1)	1.99(8)	10
	1290(2)	123.0(2)	197.8(2)	0.74(2)	3.09(8)	200
	1589(5)	151.5(4)	219.6(3)			300
$B \parallel b$ axis	1330(3)	126.8(3)	200.9(2)			120
	1524(5)	145.3(5)	215.1(3)			145
$B \parallel b \times c$ axis	135(3)	12.9(3)	64.0(7)			10
	458(4)	43.7(4)	117.9(5)			109
	1909(3)	182.0(3)	240.7(2)			209

The magnetization measurement of the $\mathrm{MoAs_2}$ crystals with field along the c axis shows a diamagnetic character with a prominent dHvA oscillation up to ∼5 K. The oscillatory part in the magnetization data was extracted by subtracting a smooth background and is plotted in Fig. 4(a) as a function of inverse magnetic field at different temperatures. The corresponding fast Fourier transform (FFT) spectrum in Fig. 4(b) reveals three fundamental frequencies: F_α [134(3) T], F_β [1290(2) T], and F_γ [1589(5) T]. The quantum oscillation frequency F is related to the extremum Fermi surface cross section A_F perpendicular to the applied field direction per the Onsager equation $F = (\phi_0/2\pi^2)A_F$. Here, ϕ_0 is the magnetic flux quantum. Using this relation, we calculated the Fermi surface cross sections for these three Fermi pockets perpendicular to the c axis (see Table I). The calculated cross sections for F_β and F_γ are the largest among the members of the XPn_2 family [16–20] as well as other TSMs and comparable to those of the newly discovered threefold-degenerate TSMs WC and MoP [45,46]. As a result, the carrier density is also expected to be much higher than in conventional semimetals, which we will discuss later. The oscillation amplitude decreases rapidly with increasing temperature due to thermal fluctuations, and the F_γ component vanishes completely above 3 K. Therefore, due to the lack of experimental points, it is not possible to study the thermal damping of the F_γ component. However, the temperature dependence of the oscillation amplitude for the F_α and F_β pockets is shown in Fig. 4(c) and fitted using the thermal damping factor of the Lifshitz-Kosevich formula,

$$R_T = \frac{(2\pi^2 k_B T/\beta)}{\sinh(2\pi^2 k_B T/\beta)}, \tag{1}$$

where $\beta = e\hbar B/m^*$. From the fitting parameters, the cyclotron effective mass m^* was calculated to be $0.37(1)m_0$ and $0.74(2)m_0$ for the F_α and F_β Fermi pockets, respectively. We also calculated the Fermi momentum k_F and Fermi velocity v_F from the quantum oscillations. All the calculated parameters are summarized in Table I.

We also observed the dHvA oscillation when the magnetic field is applied along the other two mutually perpendicular directions, i.e., along the b axis and the $b \times c$ axis (see the Appendix, Fig. 9). From the comparison of the FFT spectrum in different directions, it is clear that the Fermi surface of $\mathrm{MoAs_2}$ is quite complex, with at least three Fermi pockets existing in the system. The Fermi surface geometry also has a large anisotropy, which is consistent with the observed anisotropic MR. The extracted frequency components and related parameters are listed in Table I. Note that we could not calculate the effective mass and Fermi velocity of the carriers for the Fermi pockets along these two directions due to the lack of experimental data, as the oscillations are rapidly suppressed with increasing temperature.

To get an estimate of the carrier density and mobility, we measured the Hall resistivity ρ_{yx} of the crystal at different temperatures. Figure 5 shows ρ_{yx} at some representative temperatures. The Hall resistivity is linear and negative at 300 K and indicates electron-type charge carriers. As temperature is decreased, ρ_{yx} shows a slightly nonlinear character at around 50 K, which is a signature of multiband transport, which is also apparent from our quantum oscillation analysis. However, ρ_{yx} remains negative throughout the measured temperature range and can be described well using the one-band model. From the slope of the curve $R_H = -\frac{1}{ne}$, the electron density n is calculated to be $4.8(2) \times 10^{21}\ \mathrm{cm^{-3}}$ at 2 K. The obtained density is at least two orders of magnitude higher than that of most TSMs and is in accordance with the large Fermi pockets, which were observed in the quantum oscillation measurements. In spite of such a high carrier density, the carrier mobility is quite large, $3.6(1) \times 10^3\ \mathrm{cm^2\,V^{-1}\,s^{-1}}$, and is comparable to that observed in different topological systems [35,36,47].

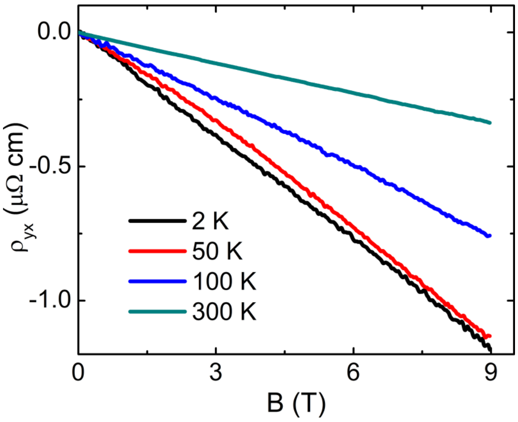

FIG. 5. Field dependence of the Hall resistivity ρ_{yx} at different temperatures.

The calculated electronic structure of $\mathrm{MoAs_2}$ is plotted in Fig. 6 along the high-symmetry directions without considering the effect of spin-orbit coupling. Even with SOC, the band structure remains almost the same. With a larger value of U and with SOC, we find some signature of a magnetic phase. The electronic structure in the low-energy spectrum is dominated by Mo d electrons. The overall electronic structure gives two large Fermi surface pockets (Fig. 7); one electron pocket, extending along the Y and F points; and a hole-Fermi-surface along the direction of Γ to X. With small tuning of the chemical potential, one can find a tiny hole pocket along Γ to Y and another electron pocket at the X points. However, these two tiny Fermi pockets are subjected to the details of the electronic

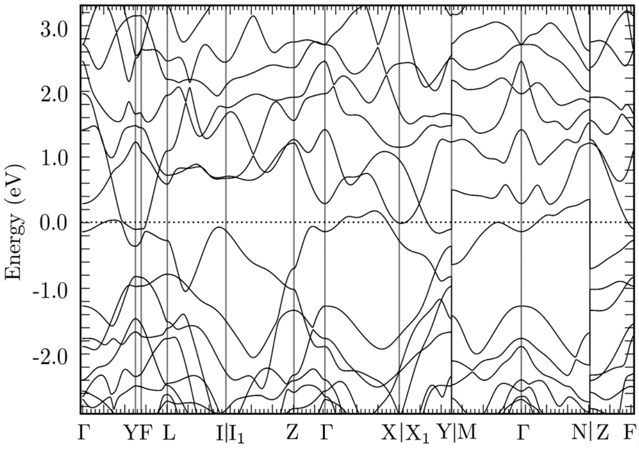

FIG. 6. The bulk band structure of $\mathrm{MoAs_2}$ without spin-orbit coupling. The Fermi energy has been aligned with $E = 0$ eV.

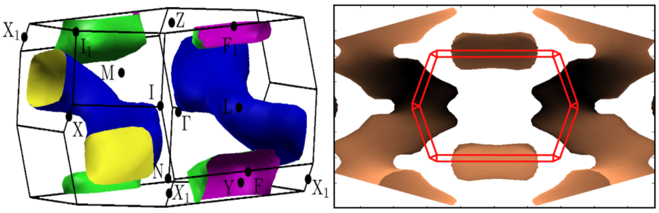

FIG. 7. The calculated Fermi surface for $MoAs_2$, showing two large Fermi pockets, including the hole-type, open-orbit Fermi surface.

structure calculation, and more importantly, they are difficult to detect. From our quantum oscillation results, we have identified at least two large and one small Fermi pockets in $MoAs_2$. On the other hand, from the Hall measurement, it is clear that the measured crystals are electron doped. Therefore, it is possible that there are two electron pockets; one large and one tiny, whereas the other large Fermi pocket is the hole type. However, the mobility of the holes must be quite small compared to that of the electrons, so that the transport is dominated only by electron-type charge carriers.

One of the interesting aspects of this material is that the hole pocket is an open-orbit Fermi surface and is strongly three-dimensional. This leads to an important question: can an open-orbit Fermi surface show quantum oscillations? We note that an open Fermi surface is also present in several organic compounds [48–54], as well as in the ortho-II phase of $YBa_2Cu_3O_{7-\delta}$ ($\delta > 0$) cuprates [55–59]. In both these materials, quantum oscillation is observed with multiple frequencies. There are also several theories modeling the origin of quantum oscillation from an open Fermi surface [60–65]. In Table I, we show the theoretically calculated Fermi surface cross sections A'_F with those obtained from the quantum oscillation measurements. Although the obtained values are comparable, there are some differences, which may occur due to several factors, such as the small deviation from perfect stoichiometry during crystal growth and various approximations for theoretical calculations. We have noticed that the theoretically overestimated cross sections are the ones arising from the open-orbit Fermi surface. For an open orbit, band renormalization plays an important role. The effective correlation strength of this band becomes larger, which may cause the reduction of its Fermi surface area. From our theoretical results, along the crystallographic b axis, we also found an additional small Fermi pocket ($A'_F = 4 \times 10^{-3}$ Å^{-2}) which is not detectable in our dHvA oscillation. This could be due to the large effective mass or lower mobility of the carriers associated with this pocket and may require higher magnetic field to resolve.

Unlike in $NbAs_2$ and $TaAs_2$ materials, $MoAs_2$'s electronic structure does not show any Dirac cone, at least not a cone which is isolated from other quadratic bands. Even for NbP, a widely studied Weyl semimetal, magnetoresistance measurements demonstrated the coexistence of linear dispersion of a Weyl cone and quadratic dispersions. The interplay between the two dispersions led to a complex experimental situation in that while some experiments claimed the existence of nontrivial Berry curvature [11,66], others found a trivial topological phase in NbP [67]. In $MoAs_2$, there might be a signature of a linear band crossing along the $X1$ to Y direction, which is about 200 meV above the Fermi level.

In spite of the trivial band structure, the magnetotransport properties in $MoAs_2$ show striking similarities with TSMs and warrant further investigation. Although there is no conclusive evidence of the origin of such a large transverse MR, a few possible explanations have been proposed. For example, in TSMs, the electronic transport through the conducting surface state is protected from backscattering by time-reversal symmetry (TRS). Under applied magnetic field, the TRS breaks and leads to increasing electron scattering, i.e., an increase in resistivity [68]. For $MoAs_2$, however, we have not found any signature of a topology-protected band structure from our first-principles calculations. In several cases, the large MR as well as the low-temperature crossover and saturation behaviors can also be described well using a semiclassical two-band model [31,32]. The large MR then appears as a consequence of compensated electron and hole density. Indeed, this model works well for understanding the observed magnetotransport properties in TMDs [16–20]. However, as is evident from the Hall resistivity, the transport properties in $MoAs_2$ are dominated by electron-type charge carriers, which is far from any electron-hole compensation scenario. Moreover, the carrier density in $MoAs_2$ is much higher than in typical TSMs and almost comparable to that of a good metal. In order to realize large MR in metals due to Lorenz force, the primary requirement is that the quantity $\omega_c\tau \gg 1$, where ω_c and τ are the cyclotron frequency and scattering time, respectively [69]. This condition typically holds in ultraclean samples, where the mean free path (i.e., mobility) of the carriers is quite large. The low residual resistivity and prominent quantum oscillation suggest that this seems to be the case in $MoAs_2$. Furthermore, for $MoAs_2$, the value of the RRR is very large and is comparable to the highest reported values for TMDs [18]. RRR is often considered as a measure of the sample quality, and the MR value usually scales with this factor [18,68]. Another important aspect is the open-orbit Fermi surface, which emerged from our theoretical calculations. As argued for the layered compound $PdCoO_2$ [70], such an open-orbit Fermi surface leads to a very small scattering rate and could also be the possible origin of the large MR value in $MoAs_2$.

V. CONCLUSIONS

To summarize the results, in this paper, we have presented a systematic study of the magnetotransport and Fermi surface properties of the transition-metal dipnictide $MoAs_2$. A field-induced resistivity plateau and large magnetoresistance have been observed, which are two of the characteristic features of a topological semimetal. The magnetoresistance shows a strong butterflylike anisotropy when the magnetic field is applied along different crystallographic directions. Unlike in other isostructural compounds, Hall measurements for $MoAs_2$ reveal a quite high carrier density with electron-type majority carriers. The Fermi surface has been probed with de Haas–van Alphen oscillation along three mutually perpendicular directions. The observed Fermi pockets are the largest among the members of the XPn_2 family and are highly anisotropic in nature. The first-principles calculations showed that the electronic band structure of $MoAs_2$ is significantly different from that of other

TMDs. The Fermi surface consists mainly of one large electron pocket and an open-orbit hole pocket, which may be the origin of such high magnetoresistance in this compound.

ACKNOWLEDGMENTS

We would like to thank A. Pal and S. Roy for their help with experimental measurements. T.D. acknowledges the financial support from the Department of Science and Technology (DST), India, under the Start Up Research Grant (Young Scientist) (SERB No. YSS/2015/001286).

APPENDIX

In Fig. 8, we have shown the angle dependence of the transverse magnetoresistance. The experimental data are fitted assuming contributions from both twofold and fourfold symmetries. Fig. 9, shows the de Haas–van Alphen oscillation for magnetic field along the *b* and *b* × *c* axes.

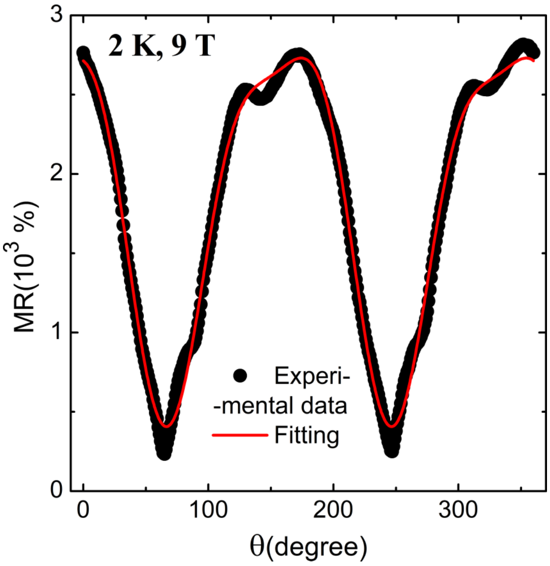

FIG. 8. Angle dependence of the transverse magnetoresistance, fitted assuming both twofold and fourfold symmetry contributions.

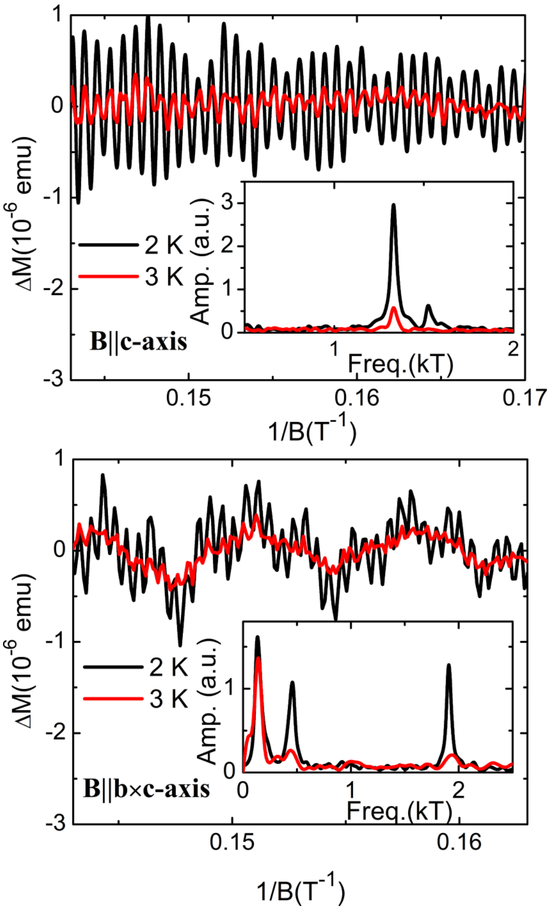

FIG. 9. The de Haas–van Alphen oscillation for magnetic field along the *b* and *b* × *c* axes. The insets show the corresponding FFT spectrum.

---

[1] H. Zhang, C.-X. Liu, X.-L. Qi, X. Dai, Z. Fang, and S.-C. Zhang, Nat. Phys. **5**, 438 (2009).

[2] Y. Xia, D. Qian, D. Hsieh, L. Wray, A. Pal, H. Lin, A. Bansil, D. Grauer, Y. S. Hor, R. J. Cava, and M. Z. Hasan, Nat. Phys. **5**, 398 (2009).

[3] Y. L. Chen, J. G. Analytis, J.-H. Chu, Z. K. Liu, S.-K. Mo, X. L. Qi, H. J. Zhang, D. H. Lu, X. Dai, Z. Fang, S. C. Zhang, I. R. Fisher, Z. Hussain, and Z.-X. Shen, Science **325**, 178 (2009).

[4] Z. K. Liu, J. Jiang, B. Zhou, Z. J. Wang, Y. Zhang, H. M. Weng, D. Prabhakaran, S.-K. Mo, H. Peng, P. Dudin, T. Kim, M. Hoesch, Z. Fang, X. Dai, Z. X. Shen, D. L. Feng, Z. Hussain, and Y. L. Chen, Nat. Mater. **13**, 677 (2014).

[5] Z. K. Liu, B. Zhou, Y. Zhang, Z. J. Wang, H. M. Weng, D. Prabhakaran, S.-K. Mo, Z. X. Shen, Z. Fang, X. Dai, Z. Hussain, and Y. L. Chen, Science **343**, 864 (2014).

[6] B. Q. Lv, N. Xu, H. M. Weng, J. Z. Ma, P. Richard, X. C. Huang, L. X. Zhao, G. F. Chen, C. E. Matt, F. Bisti, V. N. Strocov, J. Mesot, Z. Fang, X. Dai, T. Qian, M. Shi, and H. Ding, Nat. Phys. **11**, 724 (2015).

[7] S.-Y. Xu, I. Belopolski, N. Alidoust, M. Neupane, G. Bian, C. Zhang, R. Sankar, G. Chang, Z. Yuan, C.-C. Lee, S.-M. Huang, H. Zheng, J. Ma, D. S. Sanchez, B. K. Wang, A. Bansil, F. Chou, P. P. Shibayev, H. Lin, S. Jia, and M. Z. Hasan, Science **349**, 613 (2015).

[8] G. Bian, T.-R. Chang, R. Sankar, S.-Y. Xu, H. Zheng, T. Neupert, C.-K. Chiu, S.-M. Huang, G. Chang, I. Belopolski, D. S. Sanchez, M. Neupane, N. Alidoust, C. Liu, B. Wang, C.-C. Lee, H.-T. Jeng, C. Zhang, Z. Yuan, S. Jia, A. Bansil, F. Chou, H. Lin, and M. Z. Hasan, Nat. Commun. **7**, 10556 (2016).

[9] L. M. Schoop, M. N. Ali, C. Straßer, A. Topp, A. Varykhalov, D. Marchenko, V. Duppel, S. S. P. Parkin, B. V. Lotsch, and C. R. Ast, Nat. Commun. **7**, 11696 (2016).

[10] M. N. Ali, J. Xiong, S. Flynn, J. Tao, Q. D. Gibson, L. M. Schoop, T. Liang, N. Haldolaarachchige, M. Hirschberger, N. P. Ong, and R. J. Cava, Nature (London) **514**, 205 (2014).

[11] C. Shekhar, A. K. Nayak, Y. Sun, M. Schmidt, M. Nicklas, I. Leermakers, U. Zeitler, Y. Skourski, J. Wosnitza, Z. Liu, Y. Chen, W. Schnelle, H. Borrmann, Y. Grin, C. Felser, and B. Yan, Nat. Phys. **11**, 645 (2015).

[12] R. Singha, A. K. Pariari, B. Satpati, and P. Mandal, Proc. Natl. Acad. Sci. USA **114**, 2468 (2017).

[13] S. A. Wolf, D. D. Awschalom, R. A. Buhrman, J. M. Daughton, S. von Molnár, M. L. Roukes, A. Y. Chtchelkanova, and D. M. Treger, Science **294**, 1488 (2001).

[14] J. E. Lenz, Proc. IEEE **78**, 973 (1990).

[15] C. Xu, J. Chen, G.-X. Zhi, Y. Li, J. Dai, and C. Cao, Phys. Rev. B **93**, 195106 (2016).

[16] K. Wang, D. Graf, L. Li, L. Wang, and C. Petrovic, Sci. Rep. **4**, 7328 (2014).

[17] B. Shen, X. Deng, G. Kotliar, and N. Ni, Phys. Rev. B **93**, 195119 (2016).

[18] Z. Yuan, H. Lu, Y. Liu, J. Wang, and S. Jia, Phys. Rev. B **93**, 184405 (2016).

[19] Y.-Y. Wang, Q.-H. Yu, P.-J. Guo, K. Liu, and T.-L. Xia, Phys. Rev. B **94**, 041103(R) (2016).

[20] Y. Li, L. Li, J. Wang, T. Wang, X. Xu, C. Xi, C. Cao, and J. Dai, Phys. Rev. B **94**, 121115(R) (2016).

[21] J. J. Murray, J. B. Taylor, and L. Usner, J. Cryst. Growth **15**, 231 (1972).

[22] G. Kresse and J. Furthmüller, Phys. Rev. B **54**, 11169 (1996).

[23] G. Kresse and D. Joubert, Phys. Rev. B **59**, 1758 (1999).

[24] P. Jensen, A. Kjekshus, and T. Skansen, Acta Chem. Scand. **20**, 403 (1966).

[25] J. M. Ziman, *Electrons and Phonons: The Theory of Transport Phenomena in Solids*, Classics Series (Oxford University Press, New York, 2001).

[26] F. F. Tafti, Q. D. Gibson, S. K. Kushwaha, N. Haldolaarachchige, and R. J. Cava, Nat. Phys. **12**, 272 (2016).

[27] S. Sun, Q. Wang, P.-J. Guo, K. Liu, and H. Lei, New J. Phys. **18**, 082002 (2016).

[28] P. M. Hall, S. Legvold, and F. H. Spedding, Phys. Rev. **116**, 1446 (1959).

[29] X. Zhang, Z. Xiao, H. Lei, Y. Toda, S. Matsuishi, T. Kamiya, S. Ueda, and H. Hosono, Chem. Mater. **26**, 6638 (2014).

[30] D. V. Khveshchenko, Phys. Rev. Lett. **87**, 206401 (2001).

[31] Y. L. Wang, L. R. Thoutam, Z. L. Xiao, J. Hu, S. Das, Z. Q. Mao, J. Wei, R. Divan, A. Luican-Mayer, G. W. Crabtree, and W. K. Kwok, Phys. Rev. B **92**, 180402(R) (2015).

[32] R. Singha, A. Pariari, B. Satpati, and P. Mandal, Phys. Rev. B **96**, 245138 (2017).

[33] Z. J. Xiang, D. Zhao, Z. Jin, C. Shang, L. K. Ma, G. J. Ye, B. Lei, T. Wu, Z. C. Xia, and X. H. Chen, Phys. Rev. Lett. **115**, 226401 (2015).

[34] N. Wakeham, E. D. Bauer, M. Neupane, and F. Ronning, Phys. Rev. B **93**, 205152 (2016).

[35] M. Novak, S. Sasaki, K. Segawa, and Y. Ando, Phys. Rev. B **91**, 041203(R) (2015).

[36] O. Pavlosiuk, P. Swatek, and P. Wisniewski, Sci. Rep. **6**, 38691 (2016).

[37] V. P. Jovanović, L. Fruchter, Z. Z. Li, and H. Raffy, Phys. Rev. B **81**, 134520 (2010).

[38] Y. Q. Zhang, H. Meng, X. W. Wang, X. Wang, H. H. Guo, Y. L. Zhu, T. Yang, and Z. D. Zhang, Appl. Phys. Lett. **97**, 172502 (2010).

[39] M. N. Ali, L. M. Schoop, C. Garg, J. M. Lippmann, E. Lara, B. Lotsch, and S. S. P. Parkin, Sci. Adv. **2**, e1601742 (2016).

[40] A. Collaudin, B. Fauqué, Y. Fuseya, W. Kang, and K. Behnia, Phys. Rev. X **5**, 021022 (2015).

[41] J. Wang, L. Li, W. You, T. Wang, C. Cao, J. Dai, and Y. Li, Sci. Rep. **7**, 15669 (2017).

[42] X. Huang, L. Zhao, Y. Long, P. Wang, D. Chen, Z. Yang, H. Liang, M. Xue, H. Weng, Z. Fang, X. Dai, and G. Chen, Phys. Rev. X **5**, 031023 (2015).

[43] Q. Li, D. E. Kharzeev, C. Zhang, Y. Huang, I. Pletikosic, A. V. Fedorov, R. D. Zhong, J. A. Schneeloch, G. D. Gu, and T. Valla, Nat. Phys. **12**, 550 (2016).

[44] J. Hu, T. F. Rosenbaum, and J. B. Betts, Phys. Rev. Lett. **95**, 186603 (2005).

[45] J. B. He, D. Chen, W. L. Zhu, S. Zhang, L. X. Zhao, Z. A. Ren, and G. F. Chen, Phys. Rev. B **95**, 195165 (2017).

[46] C. Shekhar, Y. Sun, N. Kumar, M. Nicklas, K. Manna, V. Süß, O. Young, I. Leermakers, T. Forster, M. Schmidt, L. Muechler, P. Werner, W. Schnelle, U. Zeitler, B. Yan, S. S. P. Parkin, and C. Felser, arXiv:1703.03736.

[47] Y. Luo, H. Li, Y. M. Dai, H. Miao, Y. G. Shi, H. Ding, A. J. Taylor, D. A. Yarotski, R. P. Prasankumar, and J. D. Thompson, Appl. Phys. Lett. **107**, 182411 (2015).

[48] S. Uji, T. Terashima, H. Aoki, J. S. Brooks, M. Tokumoto, N. Kinoshita, T. Kinoshita, Y. Tanaka, and H. Anzai, Phys. Rev. B **54**, 9332 (1996).

[49] P. Auban-Senzier, A. Audouard, V. N. Laukhin, R. Rousseau, E. Canadell, L. Brossard, D. Jérome, and N. D. Kushch, J. Phys. I France **5**, 1301 (1995).

[50] E. Ohmichi, H. Ito, T. Ishiguro, G. Saito, and T. Komatsu, Phys. Rev. B **57**, 7481 (1998).

[51] H. Weiss, M. V. Kartsovnik, W. Biberacher, E. Steep, E. Balthes, A. G. M. Jansen, K. Andres, and N. D. Kushch, Phys. Rev. B **59**, 12370 (1999).

[52] P. M. Chaikin, M. Ya. Azbel, M. J. Naughton, R. V. Chamberlin, X. Yan, S. Hsu, and L. Y. Chiang, Synth. Met. **27**, B163 (1988).

[53] A. V. Kornilov, V. M. Pudalov, A.-K. Klehe, A. Ardavan, J. S. Qualls, and J. Singleton, Phys. Rev. B **76**, 045109 (2007).

[54] A. V. Korndov, V. M. Pudalov, A.-K. Klehe, A. Ardavan, J. S. Quails, and J. Singleton, J. Low Temp. Phys. **142**, 305 (2006).

[55] N. D. Leyraud, C. Proust, D. LeBoeuf, J. Levallois, J.-B. Bonnemaison, R. Liang, D. A. Bonn, W. N. Hardy, and L. Taillefer, Nature (London) **447**, 565 (2007).

[56] J. Singleton, C. de la Cruz, R. D. McDonald, S. Li, M. Altarawneh, P. Goddard, I. Franke, D. Rickel, C. H. Mielke, X. Yao, and P. Dai, Phys. Rev. Lett. **104**, 086403 (2010).

[57] S. E. Sebastian, N. Harrison, P. A. Goddard, M. M. Altarawneh, C. H. Mielke, R. Liang, D. A. Bonn, W. N. Hardy, O. K. Andersen, and G. G. Lonzarich, Phys. Rev. B **81**, 214524 (2010).

[58] S. E. Sebastian, N. Harrison, M. M. Altarawneh, C. H. Mielke, R. Liang, D. A. Bonn, W. N. Hardy, and G. G. Lonzarich, Proc. Natl. Acad. Sci. USA **107**, 6175 (2010).

[59] E. A. Yelland, J. Singleton, C. H. Mielke, N. Harrison, F. F. Balakirev, B. Dabrowski, and J. R. Cooper, Phys. Rev. Lett. **100**, 047003 (2008).

[60] P. S. Varma and T. Das, arXiv:1602.05269.

[61] R. W. Start and R. Reifenberger, J. Low. Temp. Phys. **26**, 763 (1976).

[62] A. B. Pippard, Proc. R. Soc. London, Ser. A **270**, 1 (1962).

[63] A. B. Pippard, Proc. R. Soc. London, Ser. A **287**, 165 (1965).

[64] M. Y. Azbel and P. M. Chaikin, Phys. Rev. Lett. **59**, 582 (1987).

[65] T. Osada and N. Miura, Solid State Commun. **69**, 1169 (1989).

[66] Z. Wang, Y. Zheng, Z. Shen, Y. Lu, H. Fang, F. Sheng, Y. Zhou, X. Yang, Y. Li, C. Feng, and Z.-A. Xu, Phys. Rev. B **93**, 121112(R) (2016).

[67] Sudesh, P. Kumar, P. Neha, T. Das, and S. Patnaik, Sci. Rep. **7**, 46062 (2017).

[68] T. Liang, Q. Gibson, M. N. Ali, M. Liu, R. J. Cava, and N. P. Ong, Nat. Mater. **14**, 280 (2015).

[69] A. A. Abrikosov, *Fundamentals of the Theory of Metals* (North-Holland, Amsterdam, 1988).

[70] H. Takatsu, J. J. Ishikawa, S. Yonezawa, H. Yoshino, T. Shishidou, T. Oguchi, K. Murata, and Y. Maeno, Phys. Rev. Lett. **111**, 056601 (2013).